
Article:
Hageman, T. and de Borst, R. orcid.org/0000-0002-3457-3574 (2020) A convergence study of monolithic simulations of flow and deformation in fractured poroelastic media. International Journal for Numerical Methods in Engineering, 121 (3). pp. 393-410. ISSN 0029-5981

https://doi.org/10.1002/nme.6213

Received: Added at production | Revised: Added at production | Accepted: Added at production

DOI: xxx/xxxx

ARTICLE TYPE

A convergence study of monolithic simulations of flow and deformation in fractured poroelastic media

Tim Hageman | René de Borst*

Department of Civil and Structural Engineering, University of Sheffield, Sheffield, UK

Correspondence
*René de Borst, Department of Civil and Structural Engineering, University of Sheffield, Sheffield S1 3JD, UK. Email: r.deborst@sheffield.ac.uk

Funding information
Horizon 2020 European Research Council Grant 664734 "PoroFrac"

Summary

A consistent linearisation has been carried out for a monolithic solution procedure of a poroelastic medium with fluid-transporting fractures, including a comprehensive assessment of the convergence behaviour. The fracture has been modelled using a sub-grid scale model with a continuous pressure across the fracture. The contributions to the tangential stiffness matrix of the fracture have been investigated to assess their impact on convergence. Simulations have been carried out for different interpolation orders and for Non-Uniform Rational B-Splines as interpolants vs Lagrangian polynomials. To increase the generality of the results, Newtonian as well as non-Newtonian (power-law) fluids have been considered. Unsurprisingly, a consistent linearisation invariably yields a quadratic convergence, but comes at the expense of a loss of symmetry and recalculation of the contribution of the interface to the stiffness matrix at each iteration. When using a linear line search however, the inclusion of only those terms of the interface stiffness which result in a symmetric and constant tangential stiffness matrix is sufficient to obtain a stable and convergent iterative process.

KEYWORDS:
Poroelasticity, fracture, monolithic solvers, convergence, Newton-Raphson method

1 | INTRODUCTION

The analysis of fluid flow in deformable, fractured porous media is of importance for a variety of applications: Hydraulic fracturing, pollutant transport and geothermal energy in geomechanics, flow through filters in chemical engineering, and blood flow through biological tissues in biomedical engineering, to name a few. These applications often require simulations of large domains, with complex interactions between the fracture, the deformable porous medium, and the interstitial fluid inside this porous medium. Commonly, behaviour of the fluid flow in the fracture is modelled using the cubic law [1,2,3,4,5,6]. This relation, based on the Reynolds equation, provides a nonlinear relation between the total fluid transported inside the fracture and the pressure gradient and opening height.

Instead of directly postulating the cubic law to describe the transport inside the fracture, the inflow and outflow of the fracture can be used to include its effect on the surrounding porous medium [7,8]. This approach encompasses a discontinuous pressure model, which allows for the inclusion of small-scale effects like boundary layers around the fracture [9,10], but also continuous pressure models for describing the fluid transport inside the fracture without requiring additional pressure degrees of freedom [11,12,13]. These models are intimately to approaches which are directly based on the use of Reynolds' equation for the fluid velocity profile inside the fracture, and do not explicitly require the simulation of fluid transport in the interior of the fracture.

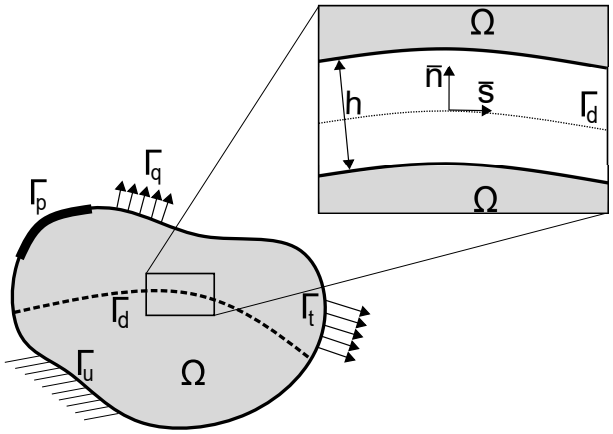

FIGURE 1 Overview of domain Ω with an internal discontinuity Γ_d and the locations of the boundaries Γ_p, Γ_q, Γ_t and Γ_u. The local $(\overline{s}, \overline{n})$ coordinate system is used for the fracture with an aperture h.

To solve the resulting system of equations for the fracture, the interstitial fluid pressure, and the deformations of the porous medium, several schemes exist. Staggered and iterative schemes have been applied successfully for the simulation of poroelastic problems[14,15,16], allowing for the combination of separate solvers developed for the fluid problem and the resolution of the displacements. Simulation of pressurised fractures in non-porous media has shown the ability of iterative schemes to yield stable solutions in spite of large nonlinearities introduced by the fracture[17,18]. This was achieved by applying an undrained hydraulic fracture split, taking into account the changes in the fluid pressure caused by the fracture opening while solving for the displacements of the solid constituent. An iterative scheme in which the interstitial fluid and fracture pressures are solved simultaneously, while iterating between these pressures and the displacements, has been used to simulate pressurised fracture propagation in poroelastic media[19,20].

Another approach is to solve simultaneously for the fluid pressure and the solid displacements, i.e. in a monolithic manner. This method, commonly implemented using a Newton-Raphson scheme, is often applied when solving poroelastic problems which contain fractures. It has been combined successfully with interface elements[2,6], the eXtended Finite Element Method (XFEM)[4,9,10,21,22], the phase-field approach[23], and isogeometric formulations[12,13]. While monolithic schemes exhibit an improved stability compared to staggered and iterative schemes, they normally result in a non-symmetric tangential stiffness matrix, which needs to be recalculated for each Newton-Raphson iteration. For this reason, Réthoré *et al.*[11,24] and Vignollet *et al.*[13] omitted most fracture-related terms in their formulation of the tangential stiffness matrix, and used a symmetric, constant stiffness matrix. Similarly, Mohammadnejad and Khoei[21] did not include inertial terms related to the fracture, and obtained a symmetric tangential stiffness matrix by scaling the mass conservation equation.

In this contribution we set out to assess the performance of a monolithic approach for resolving fluid flow and deformation in fractured porous media. To this end we will derive the contributions to the tangential stiffness matrix which relate to the fracture, and augment the tangential stiffness matrix with these terms on a one by one basis. We will then highlight the importance of the different contributions to the tangential stiffness matrix that stem from the discontinuity, in particular of those terms that are not constant and destroy the symmetry. In many of the quoted application areas, the interstitial fluid is non-Newtonian, and we will therefore extend our assessment also to these fluids. Furthermore, the effect of the increased inter-element continuity obtained by Non-Uniform Rational B-Splines (NURBS) compared to conventional Lagrange interpolation functions will be analysed, as well as the influence of the interpolation order of NURBS.

In the remainder of this paper, we first briefly summarise the governing equations for the bulk and for the continuous pressure sub-grid model. Next, attention is given to the discretisation of the governing equations in Section 3, and to the monolithic Newton-Raphson scheme used to solve the discretised equations and the derivation of the resulting tangential stiffness matrices. A typical boundary value problem containing a single fracture is simulated next, and the convergence behaviour is assessed, including the effects of an increased inter-element continuity. Section 6 presents a more complicated case with three fractures. Finally, a power-law fluid is used to investigate the effect of the interaction between the nonlinearities in the fracture and the bulk.

2 | GOVERNING EQUATIONS

We consider a domain Ω, with an internal discontinuity Γ_d, as shown in Figure 1. Across the internal discontinuity, the displacements are C^{-1} continuous, while the interstitial fluid pressure is C^0 continuous. This corresponds to the continuous pressure model for fluid flow in fractured porous media[8,25]. In the remainder of this Section we will provide a succinct overview of this model for Newtonian[11,13,7] and for non-Newtonian (power-law)[26] fluids.

2.1 | Bulk material

We assume that the deformations of the porous material occur fast compared to the fluid flow and the pressure changes. This allows the displacements in the domain Ω to be modelled as a quasi-static process by using the hydrostatic momentum balance:

$$\boldsymbol{\nabla} \cdot \boldsymbol{\sigma} = \mathbf{0} \qquad \boldsymbol{x} \in \Omega \tag{1}$$

with $\boldsymbol{\sigma}$ the total stress tensor, subject to the boundary conditions

$$\boldsymbol{u} = \overline{\boldsymbol{u}} \qquad \boldsymbol{x} \in \Gamma_u \tag{2a}$$

$$\boldsymbol{n} \cdot \boldsymbol{\sigma} = \overline{\boldsymbol{t}} \qquad \boldsymbol{x} \in \Gamma_t \tag{2b}$$

$$\boldsymbol{n}_d \cdot \boldsymbol{\sigma} = \boldsymbol{t}_{\Gamma_d} \qquad \boldsymbol{x} \in \Gamma_d \tag{2c}$$

with $\boldsymbol{u}$ the displacements of the porous material, $\overline{\boldsymbol{u}}$ the prescribed displacement on Γ_u, $\overline{\boldsymbol{t}}$ the prescribed traction on the boundary Γ_t with normal $\boldsymbol{n}$, and $\boldsymbol{t}_{\Gamma_d}$ the traction at interior discontinuity Γ_d. The total stress $\boldsymbol{\sigma}$ for a fully saturated porous material is defined as:

$$\boldsymbol{\sigma} = \boldsymbol{\sigma}_s - \alpha p \boldsymbol{I} \tag{3}$$

with α the Biot coefficient, p the pressure of the interstitial fluid, and $\boldsymbol{\sigma}_s$ the effective stress. Using a linear-elastic stress-strain relation for the solid, $\boldsymbol{\sigma}_s = \boldsymbol{D} : \boldsymbol{\varepsilon}$ with $\boldsymbol{D}$ the fourth-order elastic stiffness tensor and $\boldsymbol{\varepsilon} = \boldsymbol{\nabla}^s \boldsymbol{u}$ the infinitesimal strain tensor, $\boldsymbol{\nabla}^s$ denoting the symmetrised gradient operator, Eq. (3) can be recast as:

$$\boldsymbol{\sigma} = \boldsymbol{D} : \boldsymbol{\varepsilon} - \alpha p \boldsymbol{I} \tag{4}$$

The pressure of the interstitial fluid is obtained from mass conservation of the fluid-solid mixture:

$$\frac{1}{M}\frac{\partial p}{\partial t} + \alpha \boldsymbol{\nabla} \cdot \dot{\boldsymbol{u}} + \boldsymbol{\nabla} \cdot \boldsymbol{q} = 0 \qquad \boldsymbol{x} \in \Omega \tag{5}$$

with the following boundary conditions:

$$p = \overline{p} \qquad \boldsymbol{x} \in \Gamma_p \tag{6a}$$

$$\boldsymbol{n} \cdot \boldsymbol{q} = \overline{q} \qquad \boldsymbol{x} \in \Gamma_q \tag{6b}$$

$$\boldsymbol{n}_d \cdot \boldsymbol{q} = \boldsymbol{n}_d \cdot \boldsymbol{q}_d \qquad \boldsymbol{x} \in \Gamma_d \tag{6c}$$

with M the Biot modulus, $\overline{p}$ the prescribed pressure on Γ_p, and $\overline{q}$ the prescribed fluid flux on Γ_q. The fluid flux due to the presence of the internal discontinuity, $\boldsymbol{q}_d$ will be detailed in Section 2.2.

For Newtonian fluids the fluid flux inside the porous medium is obtained from Darcy's relation:

$$\boldsymbol{q} = -\frac{k}{\mu}\boldsymbol{\nabla} p \tag{7}$$

in which k is the intrinsic permeability of the porous material and μ is the viscosity of the fluid. For non-Newtonian fluids the fluid flux is obtained from :

$$\boldsymbol{q} = -k_f^* \left|\boldsymbol{\nabla} p\right|^{\frac{1}{n}-1} \boldsymbol{\nabla} p \tag{8}$$

with n the non-Newtonian power law index, $n < 1$ indicating a shear-thinning fluid, $n = 1$ a Newtonian fluid (in which case the expression degenerates to Eq. (7)), and $n > 1$ a shear-thickening fluid. The effective permeability is defined as:

$$k_f^* = \frac{n}{3n+1}\left(\frac{50}{3}k\right)^{\frac{1+n}{2n}} \left(2C\mu_0\right)^{-\frac{1}{n}} n_f^{\frac{n-1}{2n}} \tag{9}$$

with n_f the porosity of the porous medium, μ_0 the base viscosity of the power-law fluid, and C a constant, normally taken as $C = \frac{50}{24}$.

2.2 | Fracture

The discontinuity is modelled using zero-thickness interface elements[6,12,13,27,28], although this could equally well have been done using an XFEM discretisation. The interface elements were a priori inserted for the fractured elements and for the non-fractured elements in the extension of the fracture. The traction at the discontinuity is given by:

$$\boldsymbol{t}_{\Gamma_d} = \boldsymbol{t}_d - p\boldsymbol{n}_d \tag{10}$$

with the traction component depending on the displacement jump $[\![\boldsymbol{u}]\!]$, as follows:

$$\boldsymbol{t}_d = \boldsymbol{D}_d [\![\boldsymbol{u}]\!] \tag{11}$$

with $\boldsymbol{D}_d$ the interface stiffness matrix. Herein we will consider interfaces which are either fully fractured, or non-fractured. In the latter case, the interface stiffness matrix degenerates to:

$$\boldsymbol{D}_d = \begin{bmatrix} k_n & 0 \\ 0 & k_s \end{bmatrix} \tag{12}$$

with k_n and k_s the stiffness values in the normal and the tangential directions, respectively, which are assigned a high value to prevent non-physical crack opening. For the fully fractured interface elements the stiffness values are zero as no cohesive zone model was used. To prevent negative fracture opening heights, the dummy stiffness k_n was assigned to the fractured elements when a negative opening occurred. Since this traction - relative displacement relation is given in the local $(\overline{s}, \overline{n})$ coordinate system, it must be rotated to the global coordinate system using the rotation matrix $\boldsymbol{R}$:

$$\overline{\boldsymbol{D}_d} = \boldsymbol{R}^T \boldsymbol{D}_d \boldsymbol{R} \tag{13}$$

For the flow inside the fracture it is assumed that the fluid is nearly incompressible. It is furthermore assumed that the fluid inside the fracture reacts fast to changes in the pressure, compared to the interstitial fluid. This allows the use of Stokes' equation to describe the velocity inside the fracture. For a Newtonian fluid this results in a parabolic velocity profile[11,13], yielding a fracture inflow given by:

$$[\![w]\!]_f = \frac{1}{12}\frac{h^3}{\mu}\frac{\partial^2 p}{\partial \overline{s}^2} + \frac{1}{4}\frac{h^2}{\mu}\frac{\partial h}{\partial \overline{s}}\frac{\partial p}{\partial \overline{s}} - h\frac{\partial v_f}{\partial \overline{s}} \tag{14}$$

with h the height of the fracture and v_f the velocity of the fluid inside the porous medium at the walls of the crack (assuming a no-slip boundary condition). The expression closely resembles Reynolds' equation for the flow of a thin layer of fluid between two walls, and corresponds to the cubic law often used to model fluid flow inside fractures[1,2,3,4,5,6]. It can be extended to non-Newtonian fluids[26] and then takes the form:

$$[\![w]\!]_f = \frac{2}{2n+1}\left(\frac{h}{2}\right)^{\frac{1}{n}+2} \mu_0^{-\frac{1}{n}} \left|\frac{\partial p}{\partial \overline{s}}\right|^{\frac{1}{n}-1} \frac{\partial^2 p}{\partial \overline{s}^2} + \left(\frac{h}{2}\right)^{\frac{1}{n}+1} \mu_0^{-\frac{1}{n}} \left|\frac{\partial p}{\partial \overline{s}}\right|^{\frac{1}{n}-1} \frac{\partial h}{\partial \overline{s}}\frac{\partial p}{\partial \overline{s}} - h\frac{\partial v_f}{\partial \overline{s}} \tag{15}$$

Clearly, the expression for a Newtonian fluid is retrieved for $n = 1$.

From local mass conservation we obtain the boundary condition for the fluid absorbed in the discontinuity:

$$\boldsymbol{n}_d \cdot \boldsymbol{q}_d = \frac{1}{2}\left([\![w_f]\!] - [\![w_s]\!]\right) \tag{16}$$

where the jump in solid velocity is given by:

$$[\![w_s]\!] = \frac{\partial h}{\partial t} \tag{17}$$

This boundary condition is applied to the top and bottom of the interface elements. Since an interface model is used in which the pressure is continuous across the fracture, the pressure at the top and bottom corresponds to the same degree of freedom. Therefore, the boundary condition is only integrated along the bottom of the interface, and applied twice to the single pressure degree of freedom at the discontinuity.

3 | DISCRETISATION

The weak forms are derived using a standard Bubnov-Galerkin method. Equation (1) is multiplied with the test function $\boldsymbol{\eta}$. Using Eq. (3) this results in:

$$\int_\Omega \nabla\boldsymbol{\eta} : (\boldsymbol{\sigma}_s - \alpha p\boldsymbol{I})d\Omega - \int_{\Gamma_d} \boldsymbol{\eta}\cdot\left(\boldsymbol{t}_d - p\boldsymbol{n}_d\right)d\Gamma = \int_{\Gamma_t} \boldsymbol{\eta}\cdot\bar{\boldsymbol{t}}\,d\Gamma \tag{18}$$

Similarly, the mass conservation equation, Eq. (5), is multiplied with the test function for the fluid ζ. Combined with the non-Newtonian fluid flux, Eq. (8) this results in:

$$\int_{\Omega} \alpha\zeta\boldsymbol{\nabla}\cdot\dot{\boldsymbol{u}}\,d\Omega + \int_{\Omega} k_f^*\,|\boldsymbol{\nabla}p|^{1/n-1}\,\boldsymbol{\nabla}\zeta\cdot\boldsymbol{\nabla}p\,d\Omega + \int_{\Omega}\frac{1}{M}\zeta\dot{p}\,d\Omega + \int_{\Gamma_d}\zeta\boldsymbol{n}_d\cdot\boldsymbol{q}_d\,d\Gamma = -\int_{\Gamma_q}\zeta\overline{q}\,d\Gamma \tag{19}$$

The spatial discretisation of the weak forms of Eqs (18) and (19) has been performed using Lagrange shape functions, commonly used in finite element methods (FEM), and also with Non-Uniform Rational B-Splines (NURBS), which are used in isogeometric analysis (IGA). The advantage of using NURBS over Lagrange shape functions is the increased inter-element continuity, with NURBS of order p having a C^{p-1} inter-element continuity, whereas Lagrange shape functions have a C^0 inter-element continuity independent of the order of the shape functions used. It has been shown that this increased continuity is required in order to obtain accurate results based on the continuous pressure model used for the fracture[26].

In order to use the Lagrange and NURBS shape functions in a similar manner, Bézier extraction has been used to cast the NURBS shape functions into a standard finite element data-structure[29]. This allows for the evaluation of the internal forces on a per-element basis, while retaining the higher order inter-element continuity. Denoting the element shape functions used for the solid displacement with $\boldsymbol{N}_s$ and the interstitial fluid pressure shape functions with $\boldsymbol{N}_f$, the pressures and displacements are discretised as:

$$\boldsymbol{u} = \sum_{e=1}^{n_{el}} \boldsymbol{N}_s^{el}\boldsymbol{u}^{el} \tag{20}$$

$$p = \sum_{e=1}^{n_{el}} \boldsymbol{N}_f^{el}\boldsymbol{p}^{el} \tag{21}$$

The formulation for the fracture inflow, Eq. (16), requires first and second spatial gradients of the pressure. Therefore, at least quadratic shape functions have to be used for the fluid in order to evaluate this term, while the use of cubic NURBS will assure a continuous fracture inflow. If, instead of including the fluid transport inside the fracture by the fracture inflow model, the fluid flow inside the fracture had directly been simulated by, for instance, the cubic law, quadratic NURBS would have sufficed to obtain continuous results for the fluid transported. In order to prevent possible oscillations, the inf-sup condition has to be fulfilled[30]. This can be achieved by using shape functions for the displacement of the solid which are an order higher than those for the fluid, thus using quartic shape functions for the displacement of the solid. In this paper, several combinations of solid and fluid shape functions have been used: Quartic NURBS for the displacement with cubic NURBS for the pressure (hereafter refered to as 4×3 IGA), cubic NURBS for both the displacement and pressure (3×3 IGA), quadratic NURBS for both the solid and fluid (2×2 IGA) and quadratic Lagrange elements for both the fluid and solid (2×2 FEM). While the equal order shape functions do not fulfil the inf-sup condition, no spurious pressure oscillations were observed in the converged solutions unless mentioned otherwise.

Using the discretisations of Eqs (20) and (21), the weak form of the momentum balance from Eq. (18) is written as:

$$\boldsymbol{f}_{ext} - \boldsymbol{f}_{int} - \boldsymbol{f}_d = 0 \tag{22}$$

with the external force defined in a standard manner as:

$$\boldsymbol{f}_{ext} = \int_{\Gamma_t} \boldsymbol{N}_s^T\bar{\boldsymbol{t}}d\Gamma \tag{23}$$

while the internal force for the interior of the domain Ω is given by:

$$\boldsymbol{f}_{int} = \int_{\Omega} \boldsymbol{B}^T\boldsymbol{\sigma}_s\,d\Omega - \int_{\Omega}\alpha\boldsymbol{B}^T\boldsymbol{m}\boldsymbol{N}_f\boldsymbol{p}^{el}\,d\Omega \tag{24}$$

with $\boldsymbol{m} = [1\ 1\ 0]^T$, and the strain-nodal displacement operator $\boldsymbol{B}$ used to map the element displacements at the control points to the strain in the integration points, defined as:

$$\boldsymbol{\varepsilon}^{el} = \boldsymbol{B}\boldsymbol{u}^{el} \tag{25}$$

To obtain the jump in displacement over the fracture, the matrix $\boldsymbol{N}_d$ is introduced:

$$[\![\boldsymbol{u}]\!]^{el} = \boldsymbol{N}_d\boldsymbol{u}^{el} \tag{26}$$

which relate the displacements $\boldsymbol{u}^{el}$ to the crack opening via $h = \boldsymbol{n}_{\Gamma_d}^T \boldsymbol{N}_d \boldsymbol{u}^{el}$. Use of this mapping allows the internal forces due to the discontinuity to be given by:

$$\boldsymbol{f}_d = \int_{\Gamma_d} \boldsymbol{N}_d^T \boldsymbol{R}^T \boldsymbol{D}_d \boldsymbol{R} \boldsymbol{N}_d \boldsymbol{u}^{el} \, d\Gamma - \int_{\Gamma_d} \boldsymbol{N}_d^T \boldsymbol{n}_{\Gamma_d} \boldsymbol{N}_f \boldsymbol{p}^{el} \, d\Gamma \tag{27}$$

To prevent traction oscillations for non-fractured elements at the discontinuity, the first terms of Eq. (27) are evaluated using lumped integration[28].

The temporal discretisation has been carried out using a backward Euler integration scheme. This requires all terms of Eq. (22) to be evaluated at $t + \Delta t$. The weak form of the mass conservation from Eq. (19) then reads:

$$\boldsymbol{q}_{ext} - \boldsymbol{q}_{int} - \boldsymbol{q}_h - \boldsymbol{q}_p = 0 \tag{28}$$

with the external flux given by:

$$\boldsymbol{q}_{ext} = \Delta t \int_{\Gamma_q} \boldsymbol{N}_f^T \bar{q} d\Gamma \tag{29}$$

and the internal fluid flux given by:

$$\boldsymbol{q}_{int} = -\int_{\Omega} \alpha \boldsymbol{N}_f^T \boldsymbol{m}^T \boldsymbol{B} \left(\boldsymbol{u}^{t+\Delta t} - \boldsymbol{u}^t \right) \, d\Omega - \int_{\Omega} \Delta t k_f^* \left| \boldsymbol{\nabla} \boldsymbol{N}_f \boldsymbol{p}^{t+\Delta t} \right|^{\frac{1}{n}-1} \left(\boldsymbol{\nabla} \boldsymbol{N}_f \right)^T \boldsymbol{\nabla} \boldsymbol{N}_f \boldsymbol{p}^{t+\Delta t} \, d\Omega - \int_{\Omega} \frac{1}{M} \boldsymbol{N}_f^T \boldsymbol{N}_f \left(\boldsymbol{p}^{t+\Delta t} - \boldsymbol{p}^t \right) \, d\Omega \tag{30}$$

In a discrete format the L^2 norm of the pressure gradient then reads:

$$\left| \boldsymbol{\nabla} \boldsymbol{N}_f \boldsymbol{p}^{t+\Delta t} \right| = \left(\left(\boldsymbol{\nabla}_1 \boldsymbol{p}^{t+\Delta t} \right)^2 + \left(\boldsymbol{\nabla}_2 \boldsymbol{p}^{t+\Delta t} \right)^2 \right)^{\frac{1}{2}} \tag{31}$$

with $\boldsymbol{\nabla}_1$ and $\boldsymbol{\nabla}_2$ the gradient operators in the Cartesian directions. The fluid flux due to the fracture opening, resulting from $[\![w_s]\!]$ in Eq. (16), is given by:

$$\boldsymbol{q}_h = -\int_{\Gamma_d} \boldsymbol{N}_f^T \boldsymbol{n}_{\Gamma_d}^T \boldsymbol{N}_d \left(\boldsymbol{u}^{t+\Delta t} - \boldsymbol{u}^t \right) \, d\Omega \tag{32}$$

and the fluid flux due to changes of the pressure-driven flow profile inside the fracture, $[\![w]\!]_f$ in Eq. (16), is given by:

$$\boldsymbol{q}_p = \int_{\Gamma_d} \Delta t \boldsymbol{N}_f^T \Bigg(\frac{2}{2n+1} \mu_0^{-\frac{1}{n}} \left(\frac{1}{2} \boldsymbol{n}_{\Gamma_d}^T \boldsymbol{N}_d \boldsymbol{u}^{t+\Delta t} \right)^{\frac{1}{n}+2} \left| \boldsymbol{\nabla} \boldsymbol{p}^{t+\Delta t} \right|^{\frac{1}{n}-1} \boldsymbol{\nabla}^2 \boldsymbol{N}_f \boldsymbol{p}^{t+\Delta t} + \mu_0^{-\frac{1}{n}} \left(\frac{1}{2} \boldsymbol{n}_{\Gamma_d}^T \boldsymbol{N}_d \boldsymbol{u}^{t+\Delta t} \right)^{\frac{1}{n}+1} \left| \boldsymbol{\nabla} \boldsymbol{p}^{t+\Delta t} \right|^{\frac{1}{n}-1} \boldsymbol{n}_{\Gamma_d}^T \boldsymbol{\nabla} \boldsymbol{N}_d \boldsymbol{u}^{t+\Delta t} \boldsymbol{\nabla} \boldsymbol{N}_f \boldsymbol{p}^{t+\Delta t} \Bigg) d\Omega \tag{33}$$

which is valid for both Newtonian (n=1) and non-Newtonian fluids. The wall velocity terms are neglected since these are assumed to be small compared to the fluid velocity inside the fracture. All the forces and fluxes have been integrated in an element-wise manner using a Gauss integration scheme, requiring the values of the shape functions and their derivatives to only be evaluated in the interior of the elements.

4 | SOLUTION PROCEDURE

The system of discretised equations is solved in a monolithic manner using a Newton-Raphson algorithm. For this, the linearised system is written as:

$$\left(\left[\boldsymbol{K}_{int} \right] + \left[\boldsymbol{K}_d \right] \right) \begin{bmatrix} d\boldsymbol{u} \\ d\boldsymbol{p} \end{bmatrix}_{i+1} = \begin{bmatrix} \boldsymbol{f}_{ext} \\ \boldsymbol{q}_{ext} \end{bmatrix} - \begin{bmatrix} \boldsymbol{f}_{int} + \boldsymbol{f}_d \\ \boldsymbol{q}_{int} + \boldsymbol{q}_p + \boldsymbol{q}_h \end{bmatrix}_i \tag{34}$$

with the tangential stiffness matrix related to the internal forces and fluxes given by:

$$\boldsymbol{K}_{int} = \begin{bmatrix} \boldsymbol{K} & \boldsymbol{Q} \\ \boldsymbol{Q}^T & \boldsymbol{C} + \boldsymbol{H} \end{bmatrix} \tag{35}$$

The sub-matrix related to the stresses caused by the deformations in Ω is given by:

$$\boldsymbol{K} = \frac{\partial \boldsymbol{f}_{int}}{\partial \boldsymbol{u}} = \int_{\Omega} \boldsymbol{B}^T \boldsymbol{D} \boldsymbol{B} d\Omega \tag{36}$$

The sub-matrix related to the coupling between the solid and the fluid, caused by the interstitial fluid pressure acting on the solid material and the deformations of the solid compressing the interstitial fluid, is given by:

$$\boldsymbol{Q} = \frac{\partial \boldsymbol{f}_{int}}{\partial \boldsymbol{p}} = \left(\frac{\partial \boldsymbol{q}_{int}}{\partial \boldsymbol{u}} \right)^T = - \int_{\Omega} \alpha \boldsymbol{B}^T \boldsymbol{m} \boldsymbol{N}_f d\Omega \tag{37}$$

The tangential stiffness sub-matrix related to the pressure capacity term of the internal fluxes reads:

$$\boldsymbol{C} = \frac{\partial \boldsymbol{q}_{c,int}}{\partial \boldsymbol{p}} = - \int_{\Omega} \frac{1}{M} \boldsymbol{N}_f^T \boldsymbol{N}_f d\Omega \tag{38}$$

and, for a non-Newtonian fluid, the sub-matrix related to the fluid diffusion can be derived as:

$$\begin{aligned} \boldsymbol{H} = \frac{\partial \boldsymbol{q}_{d,int}}{\partial \boldsymbol{p}} = &- \int_{\Omega} k_f^* \Delta t \left| \boldsymbol{\nabla} \boldsymbol{N}_f \boldsymbol{p} \right|^{\frac{1}{n}-1} \left(\boldsymbol{\nabla} \boldsymbol{N}_f \right)^T \boldsymbol{\nabla} \boldsymbol{N}_f d\Omega \\ &- \int_{\Omega} k_f^* \Delta t \left(\frac{1}{n} - 1 \right) \left| \boldsymbol{\nabla} \boldsymbol{N}_f \boldsymbol{p} \right|^{\frac{1}{n}-3} \left(\boldsymbol{\nabla} \boldsymbol{N}_f \right)^T \left(\boldsymbol{\nabla} \boldsymbol{N}_f \boldsymbol{p} \right) \Big(\left(\boldsymbol{\nabla}_1 \boldsymbol{N}_f \boldsymbol{p} \right) \boldsymbol{\nabla}_1 \boldsymbol{N}_f + \left(\boldsymbol{\nabla}_2 \boldsymbol{N}_f \boldsymbol{p} \right) \boldsymbol{\nabla}_2 \boldsymbol{N}_f \Big) d\Omega \end{aligned} \tag{39}$$

For a Newtonian fluid, $n = 1$, the latter sub-matrix can be simplified to yield:

$$\boldsymbol{H} = - \int_{\Omega} \frac{k \Delta t}{\mu} \left(\boldsymbol{\nabla} \boldsymbol{N}_f \right)^T \boldsymbol{\nabla} \boldsymbol{N}_f d\Omega \tag{40}$$

As can be seen from Eqs (36) - (40), all the tangential stiffness terms related to the domain Ω are linear in the case of a Newtonian fluid. This indicates that the fluxes and forces will be exactly resolved in one iteration in the absence of discontinuities. When a discontinuity is present, the nonlinear behaviour of the system is thus solely determined by the tangential stiffness terms related to the discontinuity:

$$\boldsymbol{K}_d = \begin{bmatrix} \frac{\partial \boldsymbol{f}_d}{\partial \boldsymbol{u}} & \frac{\partial \boldsymbol{f}_d}{\partial \boldsymbol{p}} \\ \frac{\partial \boldsymbol{q}_h}{\partial \boldsymbol{u}} + \frac{\partial \boldsymbol{q}_p}{\partial \boldsymbol{u}} & \frac{\partial \boldsymbol{q}_p}{\partial \boldsymbol{p}} \end{bmatrix} \tag{41}$$

In what follows, the sub-matrices of Eq. (41) will be added one by one, in order to show the effect of including certain phenomena in the tangential stiffness matrix on the convergence of the total system.

The first term, present in all cases, is the contribution due to the interface stiffness:

$$\frac{\partial \boldsymbol{f}_d}{\partial \boldsymbol{u}} = \int_{\Gamma_d} \boldsymbol{N}_d^T \boldsymbol{R}^T \boldsymbol{D}_d \boldsymbol{R} \boldsymbol{N}_d d\Gamma \tag{42}$$

This term must be present in all simulations since it constrains the non-fractured elements from opening, thereby preventing free-body motion in part of the domain. Since this is the only complete term that can be included without rendering the tangential stiffness matrix non-symmetric, this was the only term included in the tangential stiffness matrix in earlier simulations with the continuous pressure model[11,13]. The next term is related to the force which results from the pressure inside the fracture:

$$\frac{\partial \boldsymbol{f}_d}{\partial \boldsymbol{p}} = - \int_{\Gamma_d} \boldsymbol{N}_d^T \boldsymbol{n}_{\Gamma_d} \boldsymbol{N}_f d\Gamma \tag{43}$$

Since this term is linear, its inclusion will result in the exact values of the displacements after each iteration based on the newly obtained pressures. Including the terms from Eqs (42) and (43) corresponds to an iterative scheme in which the fracture inflow is calculated based on the old displacements and pressures. This inflow is then assumed constant, and the new displacements and interstitial fluid pressures are calculated. In the case of an impermeable porous medium, this corresponds to the $P \rightarrow W$/drained hydraulic fracturing split[17,18].

Next, we add the sub-matrix which is related to the fluid absorbed from the surrounding porous medium due to opening of the fracture:

$$\frac{\partial \boldsymbol{q}_h}{\partial \boldsymbol{u}} = -\int_{\Gamma_d} \boldsymbol{N}_f^T \boldsymbol{n}_{\Gamma_d}^T \boldsymbol{N}_d d\Gamma = \left(\frac{\partial \boldsymbol{f}_d}{\partial \boldsymbol{p}}\right)^T \tag{44}$$

Since this sub-matrix is the transpose of Eq. (43), inclusion of these matrices preserves symmetry, with the concomitant advantages in computational efficiency and storage. It is also important to note that for a Newtonian fluid, these terms as well as the terms related to the interior of the domain are constant, and therefore only require to be calculated once. Since Eq. (44) is linear, it exactly accounts for the pressure changes caused by fluid being absorbed due to the opening of the fracture. This is comparable to the undrained hydraulic fracturing split, which has improved convergence and stability compared to the drained split[18].

Finally, terms are added related to the fluid which is absorbed from the porous medium due to changes in velocity profile inside the fracture:

$$\begin{aligned}\frac{\partial \boldsymbol{q}_p}{\partial \boldsymbol{p}} = &\int_{\Gamma_d} \frac{2\Delta t}{2n+1}\mu_0^{-\frac{1}{n}}\left(\frac{1}{2}\boldsymbol{n}_{\Gamma_d}^T\boldsymbol{N}_d\boldsymbol{u}\right)^{\frac{1}{n}+2}\left|\boldsymbol{\nabla}\boldsymbol{N}_f\boldsymbol{p}\right|^{\frac{1}{n}-1}\boldsymbol{N}_f^T\boldsymbol{\nabla}^2\boldsymbol{N}_f d\Gamma \\ &+\int_{\Gamma_d}\frac{2\Delta t}{2n+1}\left(\frac{1}{n}-1\right)\mu_0^{-\frac{1}{n}}\left(\frac{1}{2}\boldsymbol{n}_{\Gamma_d}^T\boldsymbol{N}_d\boldsymbol{u}\right)^{\frac{1}{n}+2}\left|\boldsymbol{\nabla}\boldsymbol{N}_f\boldsymbol{p}\right|^{\frac{1}{n}-2}\boldsymbol{\nabla}^2\boldsymbol{N}_f\boldsymbol{p}\boldsymbol{N}_f{}^T\boldsymbol{\nabla}\boldsymbol{N}_f\cdot\operatorname{sgn}\left(\boldsymbol{\nabla}\boldsymbol{N}_f\boldsymbol{p}\right)d\Gamma \\ &+\int_{\Gamma_d}\frac{\Delta t}{n}\mu_0^{-\frac{1}{n}}\left|\boldsymbol{\nabla}\boldsymbol{N}_f\boldsymbol{p}\right|^{\frac{1}{n}-1}\left(\frac{1}{2}\boldsymbol{n}_{\Gamma_d}^T\boldsymbol{N}_d\boldsymbol{u}\right)^{\frac{1}{n}+1}\left(\boldsymbol{n}_{\Gamma_d}^T\boldsymbol{\nabla}\boldsymbol{N}_d\boldsymbol{u}\right)\boldsymbol{N}_f{}^T\boldsymbol{\nabla}\boldsymbol{N}_f d\Gamma\end{aligned} \tag{45}$$

and

$$\begin{aligned}\frac{\partial \boldsymbol{q}_p}{\partial \boldsymbol{u}} = &\int_{\Gamma_d}\frac{\Delta t}{n}\mu_0^{-\frac{1}{n}}\left|\boldsymbol{\nabla}\boldsymbol{N}_f\boldsymbol{p}\right|^{\frac{1}{n}-1}\boldsymbol{\nabla}^2\boldsymbol{N}_f\boldsymbol{p}\left(\frac{1}{2}\boldsymbol{n}_{\Gamma_d}^T\boldsymbol{N}_d\boldsymbol{u}\right)^{\frac{1}{n}+1}\boldsymbol{N}_f^T\boldsymbol{n}_{\Gamma_d}^T\boldsymbol{N}_d d\Gamma_d \\ &+\int_{\Gamma_d}\Delta t\mu_0^{-\frac{1}{n}}\left|\boldsymbol{\nabla}\boldsymbol{N}_f\boldsymbol{p}\right|^{\frac{1}{n}-1}\boldsymbol{\nabla}\boldsymbol{N}_f\boldsymbol{p}\left(\frac{1}{2}\boldsymbol{n}_{\Gamma_d}^T\boldsymbol{N}_d\boldsymbol{u}\right)^{\frac{1}{n}+1}\boldsymbol{N}_f^T\boldsymbol{n}_{\Gamma_d}^T\boldsymbol{\nabla}\boldsymbol{N}_d d\Gamma \\ &+\int_{\Gamma}\frac{\Delta t}{2}\left(\frac{1}{n}+1\right)\mu_0^{-\frac{1}{n}}\left|\boldsymbol{\nabla}\boldsymbol{N}_f\boldsymbol{p}\right|^{\frac{1}{n}-1}\boldsymbol{\nabla}\boldsymbol{N}_f\boldsymbol{p}\left(\frac{1}{2}\boldsymbol{n}_{\Gamma_d}^T\boldsymbol{N}_d\boldsymbol{u}\right)^{\frac{1}{n}}\left(\boldsymbol{n}_{\Gamma_d}\boldsymbol{\nabla}\boldsymbol{N}_d\boldsymbol{u}\right)\boldsymbol{N}_f^T\boldsymbol{n}_{\Gamma_d}^T\boldsymbol{N}_d d\Gamma\end{aligned} \tag{46}$$

with sgn(·) the signum function. Including the latter two terms results in a complete and consistently linearised tangential stiffness matrix. Different from the previous terms, these two contributions are strongly dependent on the displacements and the pressure, and therefore need to be recalculated for each Newton-Raphson iteration, also for Newtonian fluids. Furthermore, including the $\partial \boldsymbol{q}_p/\partial \boldsymbol{u}$ term results in a non-symmetric tangential stiffness matrix. For a Newtonian fluid Eqs (45) and (46) can be simplified to yield:

$$\frac{\partial \boldsymbol{q}_p}{\partial \boldsymbol{p}} = \int_{\Gamma_d}\frac{\Delta t}{12\mu}\left(\boldsymbol{n}_{\Gamma_d}^T\boldsymbol{N}_d\boldsymbol{u}\right)^3\boldsymbol{N}_f^T\boldsymbol{\nabla}^2\boldsymbol{N}_f d\Gamma + \int_{\Gamma_d}\frac{\Delta t}{4\mu}\left(\boldsymbol{n}_{\Gamma_d}^T\boldsymbol{N}_d\boldsymbol{u}\right)^2\left(\boldsymbol{n}_{\Gamma_d}^T\boldsymbol{\nabla}\boldsymbol{N}_d\boldsymbol{u}\right)\boldsymbol{N}_f{}^T\boldsymbol{\nabla}\boldsymbol{N}_f d\Gamma \tag{47}$$

$$\begin{aligned}\frac{\partial \boldsymbol{q}_p}{\partial \boldsymbol{u}} = &\int_{\Gamma_d}\frac{\Delta t}{4\mu}\boldsymbol{\nabla}^2\boldsymbol{N}_f\boldsymbol{p}\left(\boldsymbol{n}_{\Gamma_d}^T\boldsymbol{N}_d\boldsymbol{u}\right)^2\boldsymbol{N}_f^T\boldsymbol{n}_{\Gamma_d}^T\boldsymbol{N}_d d\Gamma_d + \int_{\Gamma_d}\frac{\Delta t}{4\mu}\boldsymbol{\nabla}\boldsymbol{N}_f\boldsymbol{p}\left(\boldsymbol{n}_{\Gamma_d}^T\boldsymbol{N}_d\boldsymbol{u}\right)^2\boldsymbol{N}_f^T\boldsymbol{n}_{\Gamma_d}^T\boldsymbol{\nabla}\boldsymbol{N}_d d\Gamma \\ &+\int_{\Gamma}\frac{\Delta t}{2\mu}\boldsymbol{\nabla}\boldsymbol{N}_f\boldsymbol{p}\left(\boldsymbol{n}_{\Gamma_d}^T\boldsymbol{N}_d\boldsymbol{u}\right)\left(\boldsymbol{n}_{\Gamma_d}\boldsymbol{\nabla}\boldsymbol{N}_d\boldsymbol{u}\right)\boldsymbol{N}_f^T\boldsymbol{n}_{\Gamma_d}^T\boldsymbol{N}_d d\Gamma\end{aligned} \tag{48}$$

The order in which these terms have been added was chosen such that after adding the second term, the solid is resolved exactly. By adding the third term, a symmetric matrix is re-obtained. The terms related to the fluid flow were added last due to their complexity and because these are the only nonlinear terms for a Newtonian fluid, therefore being computationally more expensive to include. The pressure derivative was added before the displacement derivative to preserve a symmetric matrix with only one of these two terms added.

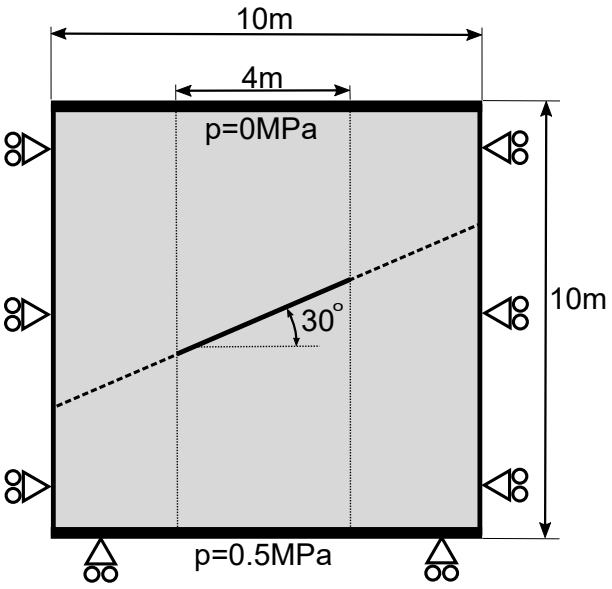

FIGURE 2 Overview of the single fracture case

To improve the convergence, a linear line search has been used in the past[31,32]. In a fluid-saturated porous medium, the factor η with which the incremental solution factor is multiplied, is determined from:

$$0 = (1-\eta)\begin{bmatrix} \boldsymbol{f}_{ext} - \boldsymbol{f}_{int} - \boldsymbol{f}_{d} \\ \boldsymbol{q}_{ext} - \boldsymbol{q}_{int} - \boldsymbol{q}_{p} - \boldsymbol{q}_{h} \end{bmatrix}_{i} \cdot \begin{bmatrix} d\boldsymbol{u} \\ d\boldsymbol{p} \end{bmatrix}_{i+1} + \eta \begin{bmatrix} \boldsymbol{f}_{ext} - \boldsymbol{f}_{int} - \boldsymbol{f}_{d} \\ \boldsymbol{q}_{ext} - \boldsymbol{q}_{int} - \boldsymbol{q}_{p} - \boldsymbol{q}_{h} \end{bmatrix}_{i+1} \cdot \begin{bmatrix} d\boldsymbol{u} \\ d\boldsymbol{p} \end{bmatrix}_{i+1} \tag{49}$$

with an upper and lower limit, $0.05 < \eta < 1.0$.

It is finally noted that the convergence of the iterative procedure is checked based on an energy criterion, with the error after iteration i defined as:

$$\epsilon_i = \begin{bmatrix} \boldsymbol{f}_{int} + \boldsymbol{f}_{d} \\ \boldsymbol{q}_{int} + \boldsymbol{q}_{p} + \boldsymbol{q}_{h} \end{bmatrix}_{i+1} \cdot \begin{bmatrix} d\boldsymbol{u} \\ d\boldsymbol{p} \end{bmatrix}_{i+1} \tag{50}$$

This energy-based criterion allocates an equal importance to the convergence of the solid deformations and the fluid pressure. While the deformations are in the order of mm ($\mathcal{O}(10^{-3})$), the pressures are in the order of MPa ($\mathcal{O}(10^{6})$). By multiplying the deformations with the forces (MPa, $\mathcal{O}(10^{6})$) and the pressures with the fluid flow (fluid flux times step size, mm $\mathcal{O}(10^{-3})$), both the momentum and mass balance convergence criteria obtain a similar magnitude. The error was normalised with the error after the first iteration, resulting in the relative error against which convergence is checked:

$$error_i = \frac{\epsilon_i}{\epsilon_1} \tag{51}$$

The simulations are considered as converged when $error_i < 10^{-6}$. If this criterion is not met after 200 iterations, the iterations are terminated when $error_{200} < 1$.

5 | CASE STUDY: A SINGLE FRACTURE

To show the effect of including the tangential stiffness terms a typical boundary-value problem is simulated[13,26]. The problem consists of a rectangular domain of 10 m × 10 m, with a discontinuity through the centre at a 30° angle, as shown in Figure 2. The centre 4 m of the discontinuity represents a fully open crack, which is not allowed to propagate. The bottom of the domain is constrained in the vertical direction, while the left-hand and the right-hand sides are constrained horizontally. A pressure difference of 0.5 MPa is applied between the bottom and top boundaries.

Simulations have been carried out using the following material parameters: Young's modulus $E = 9$ GPa, Poisson ratio $\nu = 0.4$, porosity $n_f = 0.3$, intrinsic permeability $k = 10^{-12}$ m^2, Biot modulus $M = 10^{18}$ MPa, Biot coefficient $\alpha = 1.0$, and a Newtonian fluid ($n = 1.0$) with a viscosity $\mu = 1$ mPa · s. $k_n = k_s = 10^2$ GPa have been used as values for the stiffnesses in the

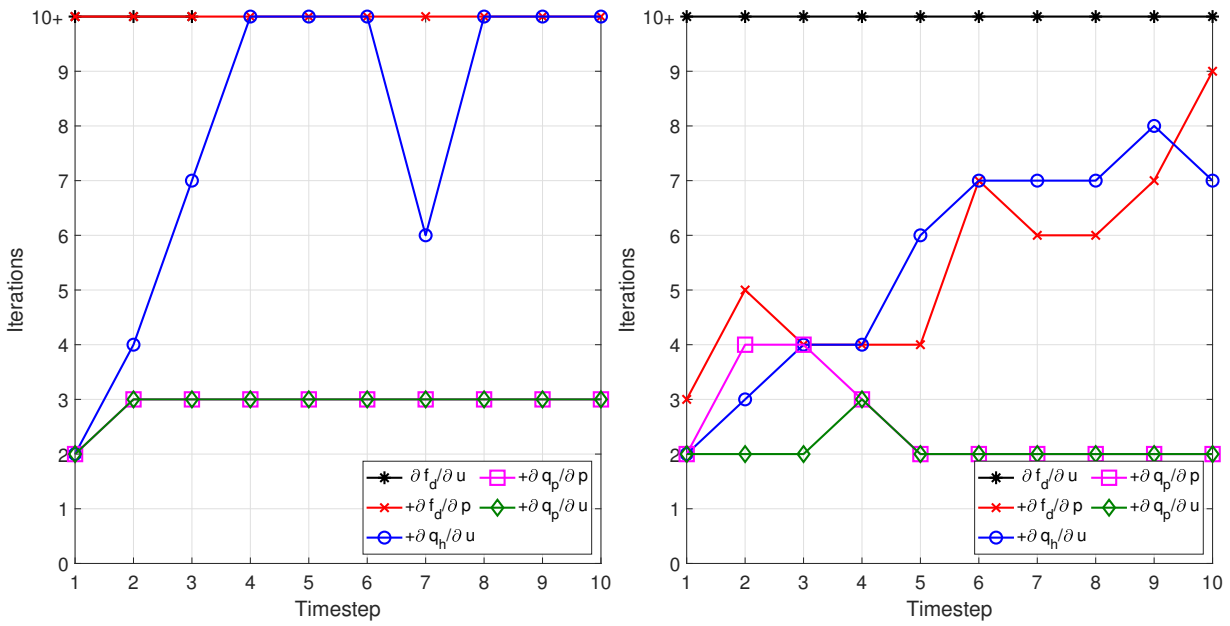

(a) Without line search **(b)** With line search

FIGURE 3 Number of iterations per time step for the case of a single fracture (4 × 3 IGA).

non-fractured interface elements. The domain has been discretised using 40 × 40 (Bézier extracted) elements, and a time-step size $\Delta t = 1$ s has been used. This mesh has been shown to be sufficiently fine to accurately resolve the influence of the fracture on the displacement and on the interstitial fluid pressure for both the isogeometric and the standard finite element analyses[26].

The tangential stiffness sub-matrices of Eq. (42) - (46) have been added on a one by one basis in the order they were introduced in Section 4 to investigate their effect on the convergence rate. Simulations have been carried out using quartic NURBS for the displacement with cubic NURBS for the interstitial pressure (4 × 3 IGA), cubic × cubic NURBS (3 × 3 IGA), quadratic × quadratic NURBS (2 × 2 IGA), and quadratic × quadratic Lagrangian finite elements (2 × 2 FEM). This allows comparing the effect of the order of the shape functions, and the effect of the increased inter-element continuity by comparing the 2 × 2 IGA results with the 2 × 2 FEM results. Even though most of the combinations of solid and fluid shape function orders do not satisfy the inf-sup condition, no spurious oscillations were observed.

5.1 | Influence of the tangential stiffness terms at the interface

We first consider a discretisation using quartic NURBS for the displacements and cubic NURBS for the pressures (4 × 3 IGA). Figure 3a shows the number of iterations for each time step, where the contributions to the interface tangential stiffness matrix have been added on a one by one basis.

When only the contribution of the stiffness is included, divergence occurs in the third time step. Inclusion of the sub-matrix related to the pressure which acts on the walls inside the fracture, $\partial \boldsymbol{f}_d / \partial \boldsymbol{p}$, results in convergence for all time-steps, but with a very large number of iterations (70-100) per time step. When we include the contribution that represents the fluid which is absorbed by the fracture, $\partial \boldsymbol{q}_h / \partial \boldsymbol{u}$ the number of iterations remains below 70 iterations, in some time steps even well below, but divergence occurs at time step 13. Inclusion of the remaining two terms yields a major improvement and consistently keeps the number of iterations below 3.

The convergence behaviour at time step 3 is shown in Figure 4. Even though all simulations converge, the oscillations in the error that occur for the $\partial \boldsymbol{f}_d / \partial \boldsymbol{u}$ case result in the simulation diverging after having reached a minimum error of $2 \cdot 10^{-2}$ in the 23$^{\text{th}}$ iteration. This behaviour is similar to convergence observed in iteratively coupled fluid-structure interaction[33,34]. In contrast, by including the $\partial \boldsymbol{f}_d / \partial \boldsymbol{p}$ term, no oscillations occur and a linear convergence rate is obtained. Including the next term result in faster convergence. However, the rate of convergence decreases and it appears to stagnate around the used convergence criterion. This behaviour has also been observed in literature for the iterative undrained hydraulic fracturing split[18]. Adding the final two terms further enhances the rate of convergence. While in both cases only three iterations were required, it can be seen

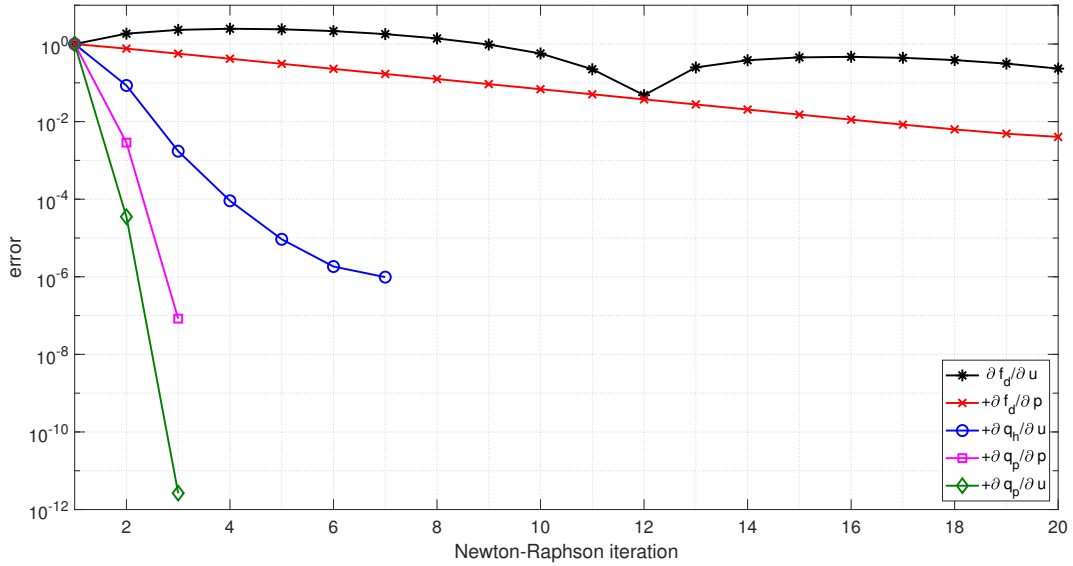

FIGURE 4 Convergence behaviour at time step 3 (4x3 IGA).

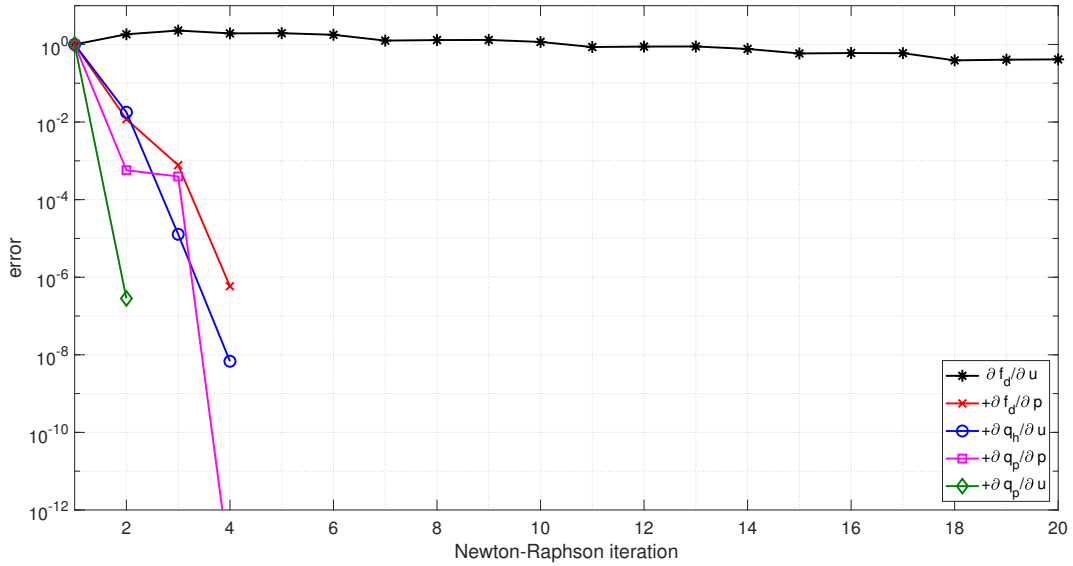

FIGURE 5 Convergence behaviour at time step 3 (4x3 IGA), with the use of a line search.

that when all the tangential stiffness sub-matrices are included the error decreases significantly faster. However, in both cases, quadratic convergence is obtained.

5.2 | Line search

We now study the effect of inclusion of a line search and show the number of iterations for each time step in 3b. With only the stiffness contribution to the tangential stiffness matrix, more than 100 iterations were needed without line search, with divergence after time step 3. The use of line searches reduces this markedly, for instance to 47 at time step 10 and 32 at time step 20. It underlines the large benefits of using line searches when using an incomplete tangential stiffness matrix. Adding the term $\partial \boldsymbol{f}_d/\partial \boldsymbol{p}$, and thereby solving for the displacements exactly, reduces the number of iterations. Adding the sub-matrix $\partial \boldsymbol{q}_h/\partial \boldsymbol{u}$ does not significantly change the situation. However, adding the last two sub-matrices again leads to a very fast convergence, with just 2 iterations at the later time steps. This is even better than results without using a line search, although the difference is

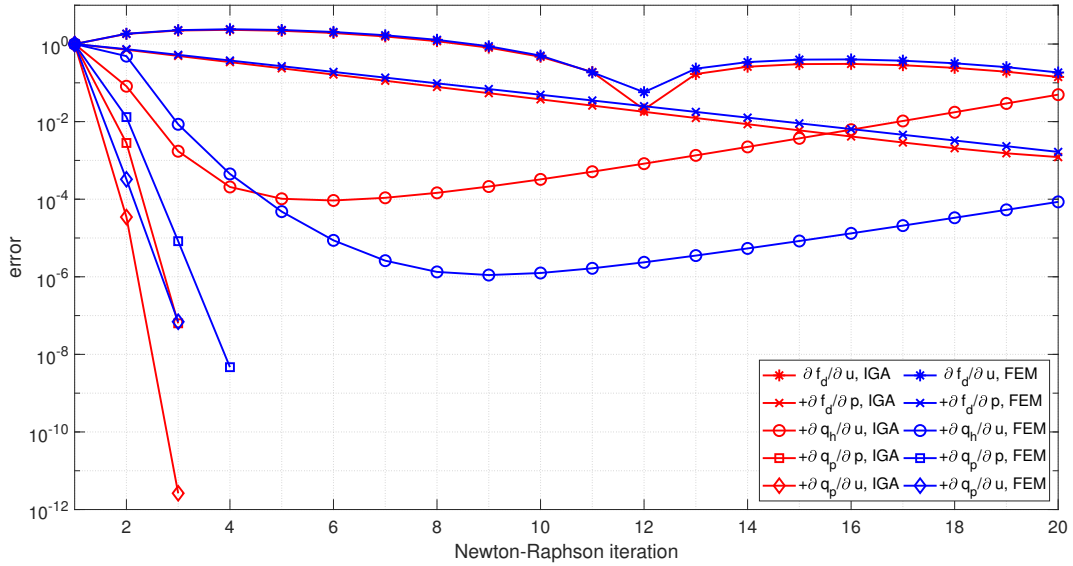

FIGURE 6 Convergence behaviour at time step 3 for 2x2 NURBS and 2x2 Lagrangian interpolations.

rather marginal, underlining that the benefits of using a line searches mainly show up when using an incomplete or inconsistent tangent operator in the Newton-Raphson process. This is also underlined in Figure 5, which shows the convergence behaviour at time step 3 when a line search is used, leading to the conclusion that the inclusion of line searches is nearly always beneficial, and can make the difference between divergence and slow convergence.

5.3 | Shape function order

A comparison of the convergence behaviour has also been carried out for different orders of interpolation, in particular between a quartic interpolation for the displacements and a cubic interpolation for the pressures, and a quadratic interpolation for both variables, using NURBS in all cases. Just small differences were found, with slightly better results for lower-order interpolations in case of an incomplete tangential stiffness matrix, but these differences vanished when all terms were included in the stiffness matrix. A similar conclusion was reached for the results with a line search.

5.4 | Interelement continuity

To investigate the possible effect of the higher interelement continuity of NURBS compared to standard Lagrange shape functions, a comparison is shown in Figure 6 when quadratic interpolations are used both for the displacements and for the pressure. While only insignificant differences are observed when only the first two sub-matrices are included, large differences occur when more terms are included, particularly when a complete or nearly complete tangential stiffness matrix is used. Using NURBS, a quadratic convergence is obtained when including the final two terms, but this is not the case when standard Lagrange interpolants are used. This indicates that the increase from a C^0 to a C^1 interelement continuity significantly improves the convergence rate, by more accurately predicting and representing the tangential stiffness terms which contain the first and the second-order derivatives of the pressure and the displacements.

Figure 7 shows the convergence when a linear line search is used. Similar to the results without line search, no difference in convergence occurs when only the $\boldsymbol{f}_d$ terms are added. When the $\boldsymbol{q}_h$ term is added, however, this changes rapidly. Including all terms again results in marked differences in convergence rate between the NURBS and the Lagrange interpolants, again indicating the beneficial effect of the enhanced interelement continuity.

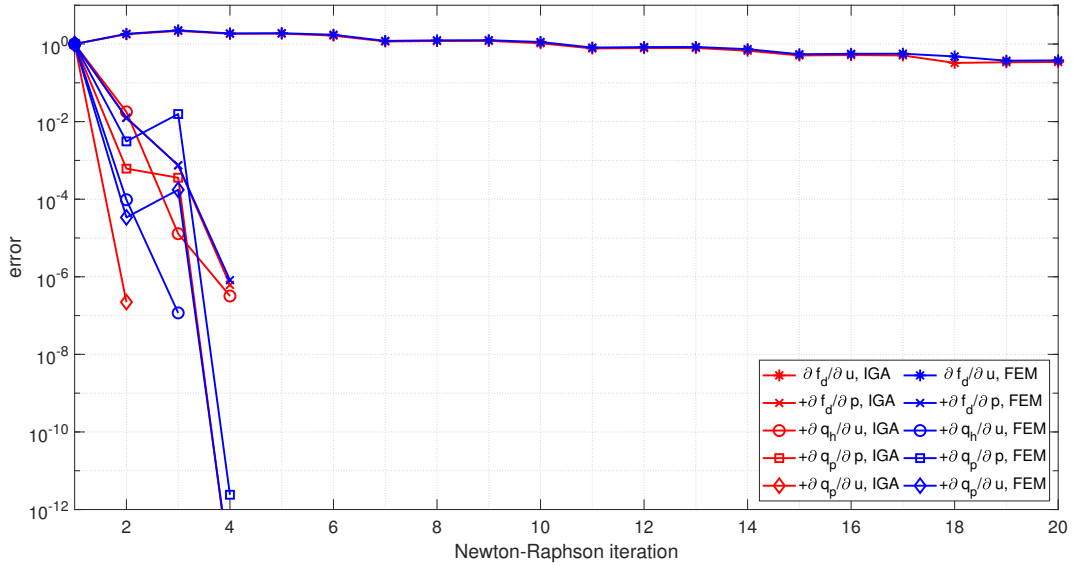

FIGURE 7 Convergence behaviour at time step 3 for 2x2 NURBS and 2x2 Lagrangian interpolations, but including the use of line searches.

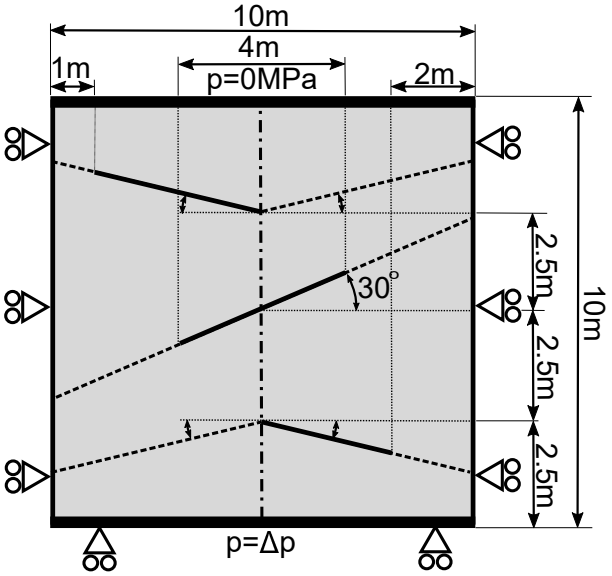

(a) Geometry and dimensions. The dotted lines show the location of the interface elements and the vertical dot-dashed line indicates the inserted C^0 continuity line. The small fractures are at an inclination angle of 15°.

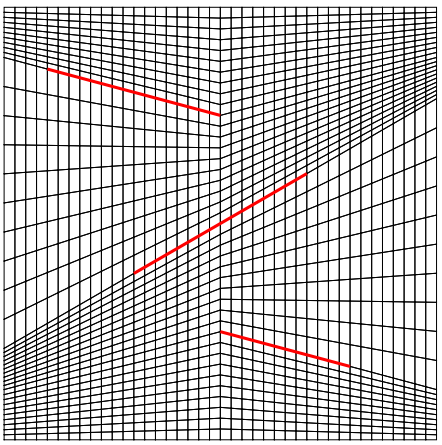

(b) The mesh, with red lines indicating the location of the fractured interface elements.

FIGURE 8 The case with three fractures.

6 | CASE WITH THREE FRACTURES

We now investigate whether the conclusions drawn before also hold for more complex cases. To this end two additional fractures are introduced, as shown in Figure 8a. The fractures are placed at a 15° angle, with a horizontal length of 3 m for the bottom fracture, and 4 m for the top fracture. In order to generate Bézier extracted NURBS meshes for this geometry, a C^0 continuity line is introduced through the centre of the domain. This allows for the sharp change in mesh direction in Figure 8b. The mesh

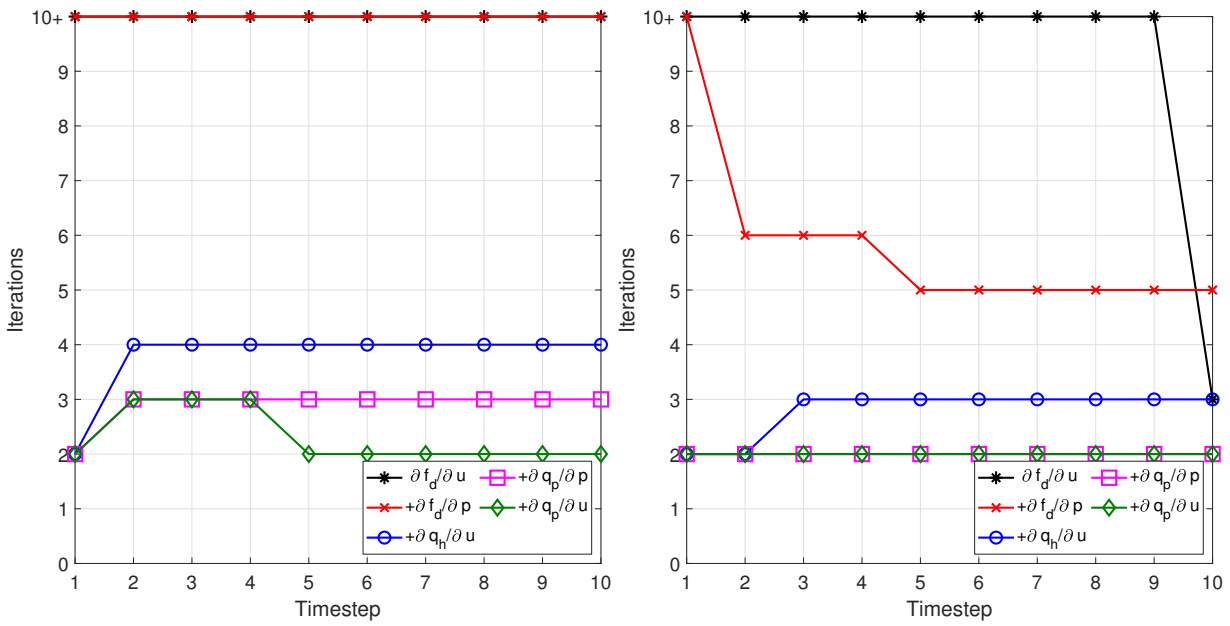

(a) 4×3 IGA, no line search applied

(b) 4×3 IGA, including line search

FIGURE 9 Number of iterations per time step for the case with three fractures, $\Delta p = 0.25$ MPa.

has 40×40 elements, similar to the case of a single fracture. The simulations have been carried out using the same properties of the solid and fluid as for the previous case, see Section 5. A constant time step size $\Delta t = 1$ s has been used and the pressure difference $\Delta p = 0.25$ MPa.

The number of iterations for the discretisation with quartic NURBS for the displacements and cubic NURBS for the pressure (4×3 IGA) is shown in Figure 9a. Both the simulation with only the $\partial \boldsymbol{f}_d / \partial \boldsymbol{u}$ sub-matrix included and the simulation including the $\partial \boldsymbol{f}_d / \partial \boldsymbol{p}$ term require 100+ iterations for all time steps. Inclusion of the sub-matrix $\partial \boldsymbol{q}_h / \partial \boldsymbol{u}$ drastically reduces the number of iterations to four, which is less than for the case of a single fracture. Including the term $\partial \boldsymbol{q}_p / \partial \boldsymbol{p}$ reduces the number of iterations to three, like in the single fracture case, and including the last term reduces the number of iterations to two for later time steps.

The number of iterations with the inclusion of a line search is shown in Figure 9b. The results are qualitatively the same as for the case of a single fracture: when only the first, constant and symmetry-preserving terms at the interface are included in the tangential stiffness matrix, a significant improvement of the convergence behaviour is observed. However, for a consistently linearised tangent stiffness operator, hardly any benefits are found, and the slight gain in number of iterations may be outweighed by the added computational costs per iteration due to the line search.

7 | NON-NEWTONIAN FLUIDS

To investigate the interaction between the tangential stiffness sub-matrices related to the fracture, and nonlinearities inside the bulk, a non-Newtonian fluid has now been considered for the geometry of Figure 8. Use of a non-Newtonian fluid yields a nonlinear behaviour also in Ω as a consequence of the nonlinear character of Equation 8. The linearisation of this relation for the fluid flux, Equation 39, has invariably been included in the tangential stiffness matrix. Simulations have been carried out for a shear-thinning fluid ($n = 0.8$), a shear-thickening fluid ($n = 1.2$), while a baseline simulation for a Newtonian fluid ($n = 1.0$) has also been included in the comparison. A base viscosity $\mu_0 = 1$ mPa $\cdot$ s^n has been used and a pressure difference $\Delta p = 0.5$ MPa The other material parameters properties have been taken as before, see Section 5. While no oscillations occur for $n = 1.0$ and $n = 1.2$ when equal-order interpolations are used, they emerge when a shear-thinning fluid ($n = 0.8$) is used. Hence, only the simulations with quartic NURBS for the displacements and cubic iterpolations for the pressure (4×3 IGA) will be compared below.

A comparison of the convergence is given in Figure 10. As for the Newtonian fluid, the simulations for the shear-thinning fluid diverge before time step 3 when the sub-matrix $\partial \boldsymbol{f}_d / \partial \boldsymbol{p}$ is omitted. In contrast, the shear-thickening fluid shows an oscillatory

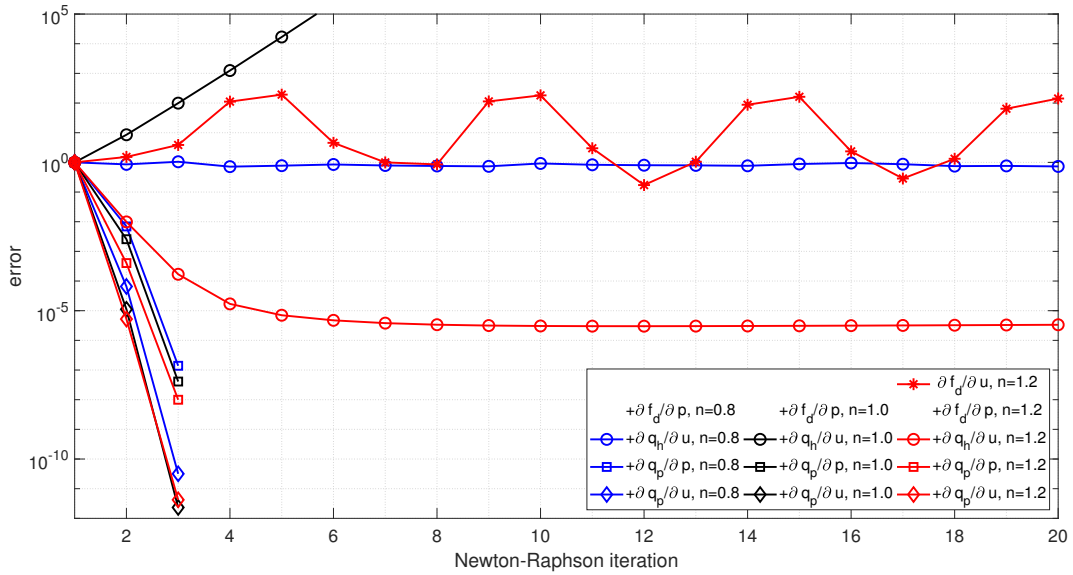

FIGURE 10 Convergence at time step 3 for two non-Newtonian fluids and a Newtonian fluid on the geometry with 3 fractures.

behaviour, but does not diverge. Similar oscillations occur for the $n = 1.0$ and $n = 1.2$ simulations with this term added, while the error for $n = 0.8$ remains fairly constant (not shown).

Adding the sub-matrix which is related to the aperture makes these oscillations disappear and improves convergence for the shear-thickening fluid. However, none of the simulations, i.e. for neither non-Newtonian fluid, and also not for the Newtonian fluid, converged. Inclusion of the last two terms results in a quadratic convergence, just like for the Newtonian fluid.

It is noted that for a consistent linearisation the simulation with the Newtonian fluid converges slightly faster compared to the non-Newtonian fluids, whereas with the last term excluded the simulation with the shear-thickening fluid converges slightly faster. These differences are small, however, indicating that the added nonlinearity does not significantly alter the convergence when all tangential stiffness sub-matrices are included. Furthermore, since the same number of iterations is required as for the Newtonian fluid, the non-Newtonian fluid behaviour can be included in the simulations without an increase in the number of iterations when all the sub-matrices are included.

A comparison between the use of NURBS and Lagrangian (quadratic equal-order) interpolations for the shear-thickening fluid ($n = 1.2$) shows that, when all sub-matrices are included, the simulations with NURBS converge significantly faster than the simulations with standard Lagrangian polynomials. This confirms that the increased inter-element connectivity of NURBS is also beneficial for the convergence rate when other nonlinearities are present.

Finally, results for shear-thinning and shear-thickening fluids using a line search are shown in Figure 11. Now, all simulations converge, but there are marked differences in convergence behaviour between both cases.

8 | CONCLUDING REMARKS

The effect of a consistent linearisation of a sub-grid model for fluid flow in fractures on the convergence of the non-linear, monolithic solver has been investigated. The sub-grid flow model is closely related to the Reynolds lubrication equation. By adding the various contributions to the tangential stiffness matrix on a one by one basis the importance of the individual terms on the convergence rate and the effect on oscillations in the convergence has been assessed. Simulations have been carried for a Newtonian fluid and for non-Newtonian fluids, yielding the same conclusions. To verify the generality of the conclusions, different geometries, including multiple fractures, were investigated.

Omitting all interface terms tends to result in divergence of the Newton-Raphson process, while a consistent linearisation, i.e. inclusion of all terms consistently yielded quadratic convergence. However, since the fracture inflow due to changes in the pressure-driven flow profile is nonlinear, this requires computing the tangential stiffness matrix at every iteration.

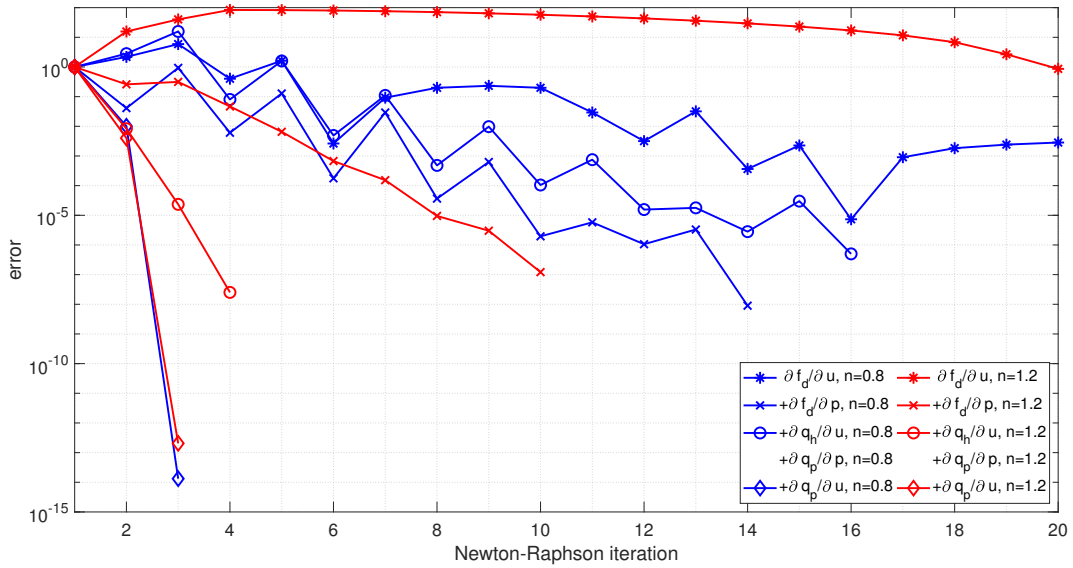

FIGURE 11 Convergence at time step 3 for a non-Newtonian fluid (n=0.8 and n=1.2) using a linear line search.

When the fracture has a relatively small influence on the interstitial pressure of the surrounding fluid, recomputing the full interface tangential stiffness matrix can be avoided by only including the effects of the interface stiffness, of the pressure acting on the walls of the fracture, and of the fluid absorbed by the terms related to the fracture opening. While this does not result in quadratic convergence, it normally yields a converging process, and preserves a symmetric and constant tangential stiffness matrix. For fracture-dominated cases, inclusion of all the tangential stiffness sub-matrices appears necessary to obtain a stable scheme if no line search is used. The use of a linear line search relaxes this requirement to the inclusion of the sub-matrices related to the momentum balance in order to obtain a stable scheme.

A comparison between simulations using quartic NURBS for the solid displacements and cubic NURBS for the interstitial fluid pressure on one hand, with simulations using quadratic NURBS for the displacements and the pressure shows that the increased order of the shape functions has near to no effect on the convergence rate. In contrast, a comparison between simulations using NURBS and standard Lagrangian shape functions shows that the increased inter-element continuity of NURBS significantly improves the convergence rate when the tangential stiffness terms contain gradients of the pressure and the fracture opening. This improved convergence of isogeometric shape functions compared to Lagrangian shape functions is irrespective whether the simulations are carried out with or without line search.

Acknowledgement
Financial support through H2020 European Research Council Advanced Grant 664734 "PoroFrac" is gratefully acknowledged.

References

1. Witherspoon PA, Wang JSY, Iwai K, Gale JE. Validity of cubic law for fluid flow in a deformable rock fracture. *Water Resources Research* 1980; 16: 1016–1024.

2. Carrier B, Granet S. Numerical modeling of hydraulic fracture problem in permeable medium using cohesive zone model. *Engineering Fracture Mechanics* 2012; 79: 312–328.

3. Gupta P, Duarte CA. Coupled hydromechanical-fracture simulations of nonplanar three-dimensional hydraulic fracture propagation. *International Journal for Numerical and Analytical Methods in Geomechanics* 2018; 42: 143–180.

4. Khoei AR, Vahab M, Haghighat E, Moallemi S. A mesh-independent finite element formulation for modeling crack growth in saturated porous media based on an enriched-FEM technique. *International Journal of Fracture* 2014; 188: 79–108.

5. Lecampion B, Bunger A, Zhang X. Numerical methods for hydraulic fracture propagation: A review of recent trends. *Journal of Natural Gas Science and Engineering* 2018; 49: 66–83.

6. Segura JM, Carol I. Coupled HM analysis using zero-thickness interface elements with double nodes. Part I: Theoretical model. *International Journal for Numerical and Analytical Methods in Geomechanics* 2008; 32: 2083–2101.

7. de Borst R. *Computational Methods for Fracture in Porous Media*. Amsterdam - Oxford - Cambridge: Elsevier . 2017.

8. de Borst R. Fluid flow in fractured and fracturing porous media: A unified view. *Mechanics Research Communications* 2017; 80: 47–57.

9. de Borst R, Réthoré J, Abellan MA. A numerical approach for arbitrary cracks in a fluid-saturated medium. *Archive of Applied Mechanics* 2006; 75: 595–606.

10. Remij EW, Remmers JJC, Huyghe JM, Smeulders DMJ. The enhanced local pressure model for the accurate analysis of fluid pressure driven fracture in porous materials. *Computer Methods in Applied Mechanics and Engineering* 2015; 286: 293–312.

11. Réthoré J, de Borst R, Abellan MA. A two-scale approach for fluid flow in fractured porous media. *International Journal for Numerical Methods in Engineering* 2007; 71: 780–800.

12. Irzal F, Remmers JJC, Verhoosel CV, de Borst R. An isogeometric analysis Bézier interface element for mechanical and poromechanical fracture problems. *International Journal for Numerical Methods in Engineering* 2014; 97: 608–628.

13. Vignollet J, May S, de Borst R. Isogeometric analysis of fluid-saturated porous media including flow in the cracks. *International Journal for Numerical Methods in Engineering* 2016; 108: 990–1006.

14. Settari A, Walters DA. Advances in coupled geomechanical and reservoir modeling with applications to reservoir compaction. *SPE Journal* 2007; 6: 334–342.

15. Kim J, Tchelepi HA, Juanes R. Stability and convergence of sequential methods for coupled flow and geomechanics: Drained and undrained splits. *Computer Methods in Applied Mechanics and Engineering* 2011; 200: 2094–2116.

16. Kim J, Tchelepi HA, Juanes R. Stability and convergence of sequential methods for coupled flow and geomechanics: Fixed-stress and fixed-strain splits. *Computer Methods in Applied Mechanics and Engineering* 2011; 200: 1591–1606.

17. Gordeliy E, Peirce A. Coupling schemes for modeling hydraulic fracture propagation using the XFEM. *Computer Methods in Applied Mechanics and Engineering* 2013; 253: 305–322.

18. Parchei Esfahani M, Gracie R. On the undrained and drained hydraulic fracture splits. *International Journal for Numerical Methods in Engineering* 2019; 118: 741–763.

19. Lee S, Wheeler MF, Wick T. Pressure and fluid-driven fracture propagation in porous media using an adaptive finite element phase field model. *Computer Methods in Applied Mechanics and Engineering* 2016; 305: 111–132.

20. Lee S, Wheeler MF, Wick T. Iterative coupling of flow, geomechanics and adaptive phase-field fracture including level-set crack width approaches. *Journal of Computational and Applied Mathematics* 2017; 314: 40–60.

21. Mohammadnejad T, Khoei AR. An extended finite element method for hydraulic fracture propagation in deformable porous media with the cohesive crack model. *Finite Elements in Analysis and Design* 2013; 73: 77–95.

22. Shi F, Wang X, Liu C, Liu H, Wu H. An XFEM-based method with reduction technique for modeling hydraulic fracture propagation in formations containing frictional natural fractures. *Engineering Fracture Mechanics* 2017; 173: 64–90.

23. Miehe C, Mauthe S. Phase field modeling of fracture in multi-physics problems. Part III. Crack driving forces in hydro-poro-elasticity and hydraulic fracturing of fluid-saturated porous media. *Computer Methods in Applied Mechanics and Engineering* 2016; 304: 619–655.

24. Réthoré J, de Borst R, Abellan MA. A two-scale model for fluid flow in an unsaturated porous medium with cohesive cracks. *Computational Mechanics* 2008; 42: 227–238.

25. Pervaiz Fathima KM, de Borst R. Implications of single or multiple pressure degrees of freedom at fractures in fluid-saturated porous media. *Engineering Fracture Mechanics* 2019; 213: 1–20.

26. Hageman T, de Borst R. Flow of non-Newtonian fluids in fractured porous media: Isogeometric vs standard finite element discretisation. *International Journal for Numerical and Analytical Methods in Geomechanics* 2019; 43: 2020–2037.

27. Schellekens JCJ, de Borst R. On the numerical integration of interface elements. *International Journal for Numerical Methods in Engineering* 1993; 36: 43–66.

28. Vignollet J, May S, de Borst R. On the numerical integration of isogeometric interface elements. *International Journal for Numerical Methods in Engineering* 2015; 102: 1733–1749.

29. Borden MJ, Scott MA, Evans JA, Hughes TJR. Isogeometric finite element data structures based on Bézier extraction of NURBS. *International Journal for Numerical Methods in Engineering* 2011; 87: 15–47.

30. Chapelle D, Bathe KJ. The inf-sup test. *Computers & Structures* 1993; 47: 537–545.

31. Crisfield MA. An arc-length method including line searches and accelerations. *International Journal for Numerical Methods in Engineering* 1983; 19: 1269–1289.

32. de Borst R, Crisfield MA, Remmmers JCJ, Verhoosel CV. *Non-Linear Finite Element Analysis of Solids and Structures*. Chichester: Wiley. second ed. 2012.

33. van Brummelen EH, de Borst R. On the nonnormality of subiteration for a fluid-structure-interaction problem. *SIAM Journal on Scientific Computing* 2005; 27: 599–621.

34. Manguoglu M, Sameh AH, Saied F, Tezduyar TE, Sathe S. Preconditioning techniques for nonsymmetric linear systems in the computation of incompressible flows. *Journal of Applied Mechanics* 2009; 76: 021204.